Revealing the kinetics of non-metallic inclusion reactions in steel using in-situ high temperature environmental scanning electron microscopy

Tuomas Alatarvas, Renaud Podor, Eetu-Pekka Heikkinen, Qifeng Shu, Harishchandra Singh

In-situ High Temperature Environmental Scanning Electron Microscopy for Probing Non-metallic Inclusions within Steel

Tuomas Alatarvas[1], Renaud Podor[2], Eetu-Pekka Heikkinen[1], Qifeng Shu[1], Harishchandra Singh[3*]

[1] Process Metallurgy Research Unit, Centre for Advanced Steels Research, University of Oulu, FIN-90014, Finland

[2] ICSM, Univ Montpellier, CEA, CNRS, ENSCM, Marcoule, France

[3] Nano and Molecular Systems Research Unit, Centre for Advanced Steels Research, University of Oulu, FIN-90014, Finland

[*] Corresponding author, harishchandra.singh@oulu.fi

Abstract

Solid-state kinetics of non-metallic inclusion (NMI) reactions in steel is gaining increasing attention, to elucidate the effect of heat treatments to NMI composition and stability. In this study, High Temperature Environmental Scanning Electron Microscope (HT-ESEM) is used for an in-situ observation of calcium aluminate complex, CaS, $MgAl_2O_4$–CaS, MnS and TiN type NMIs in steels at 800°C and 900°C for varying holding times. Together with visual morphological variations in NMIs, CaS and MnS fractions are found to decrease, promoting void formation in addition to the ferrite–austenite phase transformation. HT-ESEM driven thermodynamic calculations were carried out with FactSage 8.2 software to estimate the NMI reactions with the residual atmosphere in the sample chamber during experiments. The modelled data provide insights into the interpretation of the experimental data.

Keywords

In-situ characterisation, HT-ESEM, Non-metallic inclusions, Steel, Thermodynamic calculations

1. Introduction

Non-metallic inclusions (NMIs) are typically oxide, sulphide and nitride particles found virtually in all steel products. It is well known that the composition, size and shape of NMIs affect various properties of the steel product, such as ductility, fatigue and corrosion resistance – in general the most demanding steel applications require inclusions smaller in size and number [1]. Majority of NMIs form in the molten steel during processing stages, for instance as a result of deoxidation reactions. The primary deoxidation product in Al-killed steels is Al_2O_3, which reacts with added calcium to form calcium aluminates in the melt before casting. Further formation and reactions of NMIs take place during casting, where steel is solidified. The driving forces for the reactions originate from the decreasing temperature and alloying element enrichment in the steel during solidification due to segregation. The most typical NMI phases in Al-killed, calcium treated steel products are oxides in the Al_2O_3–CaO–MgO system, e.g., calcium aluminates with varying compositions and $MgAl_2O_4$ spinel, as well as calcium sulphide (CaS), manganese sulphide (MnS) and titanium nitride (TiN). In many cases, multiphase non-metallic inclusions are observed, i.e., a combination of two or more phases [2].

Despite the fact that most of the reactions involving NMIs occur in molten steel or during solidification, the kinetics of solid-state reactions have gained increasing attention during the recent years to assess the effect of heat treatments to NMI composition. Cheng et al. [3] investigated the transformation of NMIs in bearing steels in temperatures of 1225–1375°C. Samples were prepared after heat treatments with varying temperatures and holding times, followed by SEM-EDS analyses. It was concluded that calcium aluminate type inclusions transformed to spinel–CaS type, due to diffusion of sulphur and aluminium and subsequent reactions between the steel matrix and the NMI. Chu et al. [4] depicted a similar reaction during heat treatment of linepipe steels in the temperature range of 1000–1400°C. Wang et al. [5] derived a kinetic model for the reactions involving MgO-Al_2O_3-CaO-CaS components and the steel matrix. As a result, Time-Diameter-Transformation contours were constructed to assess the NMI composition over heating time. Liu & Webler [6,7] also reported the reactions of dissolved Mn with CaS in inclusions, promoting the formation of solid solution (Ca,Mn)S phase in CaS and MgO–Al_2O_3–CaO(–CaS) type NMIs. Until recently, there has been a lack of an in-situ observation of the solid-state NMI reactions. Liu et al. [8] investigated NMI reactions in temperatures of 1000–1200°C using in-situ confocal laser scanning microscopy, verified by SEM-EDS analyses. Uniform composition CaO–MgO–Al_2O_3 NMIs were found to transform to CaO–MgO–Al_2O_3 with an outer layer of CaS.

Recently, HT-ESEM (High Temperature Environmental Scanning Electron Microscopy) has proven itself a versatile tool, owing to its in-situ imaging and analysis in controlled atmospheres and elevated temperatures [9]. In steel research, the investigated topics include morphology and structure transformation of Al–Si coated boron steel [10] and oxidation of Co-Ce coated interconnect steel [11], however, still lack in NMI research.

The current study demonstrates the applicability of HT-ESEM for in-situ observation of solid-state non-metallic inclusion reactions occurring during heat treatment of low-alloyed steel. First, reactions between the phases within NMIs can be considered, secondly, reactions between steel matrix and NMIs, and thirdly, reactions between NMIs and residual atmosphere in the HT-ESEM sample chamber in high vacuum. To the best knowledge of the authors, no similar experiments have

been reported earlier. To support the findings, thermodynamic calculations were carried out to assess the stability of NMI phases at elevated temperatures and under high vacuum.

2. Materials and methods

2.1 Investigated materials

In this study, several non-metallic inclusions in industrial samples of low-carbon, aluminium killed and calcium treated steels in hot rolled condition were investigated. The samples, with a nominal composition of 0.15 C, 0.3 Si, 1.0 Mn, 0.4 Cr in wt%, were machined into disks with an approximate diameter of 5 mm and a thickness of 0.2 mm. Before the characterisation of NMIs, the sample surfaces were polished with a 1 µm diamond paste, and finally polished to the mirror grade using a colloidal silica solution. Non-metallic inclusions of interest were manually searched on the sample surfaces.

2.2 High Temperature Environmental Scanning Electron Microscopy

A QUANTA 200 Environmental Scanning Electron Microscope (FEI company, Netherlands) was used to perform the SEM characterizations as well as the in-situ experiments at high temperature [9]. It is equipped with a FurnaSEM 1300 furnace (NewTEC company, France) that allows to heat the samples up to 1300°C with a maximum 100°C/min heating rate [12]. High temperature backscattered electron (BSE) images were collected using a Karmen detector (Crytur company, Czech Republic) [13]. The SEM is also equipped with a Bruker SDD XFlash® 5010 Energy Dispersive X-Ray Spectrometer (EDS) with a 123 eV resolution at the Mn Kα line.

The experimental procedure for the HT-ESEM experiments is as follows. First, EDS elemental maps of the NMIs of interest were recorded before the experiment. Then, the sample was heated up to the experimental temperature (i.e. 800°C and 900°C) for various holding times. During the isothermal heat treatment, BSE images were recorded regularly to observe the NMI structural variations with a submicrometric resolution. Recorded image material was also converted to video format files, available as supplementary material. After the cooling of the sample to room temperature, EDS elemental maps of the same NMIs of interest were recorded again. The BSE images were recorded at high temperature with an 18 kV acceleration voltage to ensure the emission of high energy backscattered electrons that can be detected by the Karmen detector. The experiments were carried out in high vacuum to prevent sample surface oxidation, typical residual pressure being in the range of 10^{-4} to 10^{-3} Pa (10^{-9} to 10^{-8} bar). The EDS maps and analyses were recorded with a 6 kV acceleration voltage. In this case, the interaction between the primary electron beam and the sample remains limited to a low volume (approx. 0.05µm^3). This yields to high resolution elemental repartition maps clearly showing the details inside the NMIs.

2.3 Computational thermodynamics

FactSage 8.2 [14] was used to assess the stability of CaS, MnS, MgO, $CaAl_2O_4$, $MgAl_2O_4$, and TiN to consider the effect of residual atmosphere of the HT-ESEM to NMIs during in-situ high temperature characterisation. For the calculations, FactPS database was selected, and the Reaction module was used to calculate equilibrium constants *K* with varying temperature (800 to 1000°C). All solid compound activities were unity. The remaining atmosphere of the sample chamber in high vacuum was assumed as high in H_2 with little inert species [15]. Equations 1–5 present the NMI component

reactions with H_2 in the residual atmosphere, whereas Equations 6–9 present their volatilisation into gaseous compounds.

$$\mathrm{CaS} + \mathrm{H_2(g)} = \mathrm{Ca(g)} + \mathrm{H_2S(g)} \quad (1)$$

$$\mathrm{MnS} + \mathrm{H_2(g)} = \mathrm{Mn(g)} + \mathrm{H_2S(g)} \quad (2)$$

$$\mathrm{MgO} + \mathrm{H_2(g)} = \mathrm{Mg(g)} + \mathrm{H_2O(g)} \quad (3)$$

$$\mathrm{CaAl_2O_4} + 4\,\mathrm{H_2(g)} = \mathrm{Ca(g)} + 2\,\mathrm{Al(g)} + 4\,\mathrm{H_2O(g)} \quad (4)$$

$$\mathrm{MgAl_2O_4} + 4\,\mathrm{H_2(g)} = \mathrm{Mg(g)} + 2\,\mathrm{Al(g)} + 4\,\mathrm{H_2O(g)} \quad (5)$$

$$2\,\mathrm{CaS} = 2\,\mathrm{Ca(g)} + \mathrm{S_2(g)} \quad (6)$$

$$2\,\mathrm{MnS} = 2\,\mathrm{Mn(g)} + \mathrm{S_2(g)} \quad (7)$$

$$2\,\mathrm{MgO} = 2\,\mathrm{Mg(g)} + \mathrm{O_2(g)} \quad (8)$$

$$2\,\mathrm{TiN} = 2\,\mathrm{Ti(g)} + \mathrm{N_2(g)} \quad (9)$$

The equilibrium constant for Equation 1 can be formulated as follows:

$$K_1 = \frac{p_{\mathrm{Ca}} \times p_{\mathrm{H_2S}}}{a_{\mathrm{CaS}} \times p_{\mathrm{H_2}}} \quad (10)$$

Considering that the molar amount of forming species Ca(g) and H_2S(g) are equal within the reaction, and their initial concentration is zero, their partial pressures are equal, and Equation 11 is obtained. Solving for partial pressure of Ca in equilibrium, Equation 12 is obtained, assuming the partial pressure of H_2 is approximately equal to the total pressure P. Reactions depicted in Equations 1–3 result in similar formulation for the partial pressure of Ca, Mn, or Mg.

$$K_1 = \frac{p_{\mathrm{Ca}}^2}{a_{\mathrm{CaS}} \times p_{\mathrm{H2}}} \quad (11)$$

$$p_{\mathrm{Ca}} = \sqrt{K_1 \times P} \quad (12)$$

For Equation 4, the equilibrium constant is written as:

$$K_4 = \frac{p_{\mathrm{Ca}} \times p_{\mathrm{Al}}^2 \times p_{\mathrm{H_2O}}^4}{a_{\mathrm{CaAl_2O_4}} \times p_{\mathrm{H_2}}^4} \quad (13)$$

In the reaction, two moles of Al(g) and four moles of H_2O(g) are formed for every mole of Ca(g), resulting in the partial pressure dependences depicted in Equations 14 and 15. Substituting into Equation 13, the equilibrium constant in Equation 16 is obtained, and finally solving for p_{Ca}, Equation 17 can be formulated. The reaction depicted in Equation 5 results in a similar formulation for the solved partial pressure.

$$p_{\mathrm{Al}} = 2p_{\mathrm{Ca}} \quad (14)$$

$$p_{\mathrm{H_2O}} = 4p_{\mathrm{Ca}} \quad (15)$$

$$K_4 = \frac{p_{\mathrm{Ca}} \times (2p_{\mathrm{Ca}})^2 \times (4p_{\mathrm{Ca}})^4}{P^4} = \frac{1024 p_{\mathrm{Ca}}^7}{P^4} \quad (16)$$

$$p_{Ca} = \sqrt[7]{\frac{K_4 P^4}{1024}} \quad (17)$$

The equilibrium constant for the reaction in Equation 6 is written as:

$$K_6 = \frac{p_{\mathrm{Ca}}^2 \times p_{\mathrm{S2}}}{a_{\mathrm{CaS}}^2} \quad (18)$$

Here, one mole of S_2(g) is formed for every two moles of Ca(g), resulting in the partial pressure dependence depicted in Equation 19. Substituting into Equation 18, the equilibrium constant in Equation 20 is obtained, and finally solving for p_{Ca}, Equation 21 can be formulated. Reactions depicted in Equations 6–9 result in similar formulation for the solved partial pressures.

$$p_{\mathrm{S2}} = \frac{1}{2} p_{\mathrm{Ca}} \quad (19)$$

$$K_6 = \frac{p_{\mathrm{Ca}}^2 \times \frac{1}{2} p_{\mathrm{Ca}}}{a_{\mathrm{CaS}}^2} = \frac{p_{\mathrm{Ca}}^3}{2a_{\mathrm{CaS}}^2} \quad (20)$$

$$p_{\mathrm{Ca}} = \sqrt[3]{K_6 \times 2a_{\mathrm{CaS}}^2} = \sqrt[3]{2K_6} \quad (21)$$

For all the considered reactions, the equations for the partial pressures of gaseous Ca, Mn, Mg, or Ti compounds are listed in Table 1.

Table 1. Resulting equations for partial pressures.

Equation	Partial pressure
(1)	$p_{\mathrm{Ca}} = \sqrt{K_1(T) \times P}$
(2)	$p_{\mathrm{Mn}} = \sqrt{K_2(T) \times P}$
(3)	$p_{\mathrm{Mg}} = \sqrt{K_3(T) \times P}$
(4)	$p_{\mathrm{Ca}} = \sqrt[7]{\frac{K_4(T) \times P^4}{1024}}$
(5)	$p_{\mathrm{Mg}} = \sqrt[7]{\frac{K_5(T) \times P^4}{1024}}$
(6)	$p_{\mathrm{Ca}} = \sqrt[3]{2K_6(T)}$
(7)	$p_{\mathrm{Mn}} = \sqrt[3]{2K_7(T)}$
(8)	$p_{\mathrm{Mg}} = \sqrt[3]{2K_8(T)}$
(9)	$p_{\mathrm{Ti}} = \sqrt[3]{2K_9(T)}$

FactSage 8.2 with FSstel database was also used to estimate the transition temperature of ferrite and austenite to fully austenite with the steel composition studied.

3. Results

3.1 In-situ NMI characterisation

The sites of interest include a number of NMI types observed in aluminium killed, calcium treated steels. Table 2 presents the experimental conditions for the NMI types of interest, including calcium aluminate complex, CaS, $MgAl_2O_4$–CaS, TiN and MnS inclusions. These NMIs are representative of the 3–10 NMIs of each type that have been observed during the experiments.

Table 2. Experimental conditions for the NMIs investigated.

Site of interest	NMI type	Length (μm)	Temperature (°C)	Holding time (min)
#1	Calcium aluminate complex	14	900	120 + 150
#2	CaS	1.5	800	120
#3	$MgAl_2O_4$–CaS	4	800	30
#4	$MgAl_2O_4$–CaS	4	900	30
#5	TiN	15	800	30
#6	TiN	3	900	30
#7	MnS	10	900	30

3.1.1 Calcium aluminate complex type

In the observed NMI, the dominant phase is calcium aluminate presented in top row of Figure 1. $MgAl_2O_4$ spinel is seen as darker shade particles within both sides of the two-part NMI. In addition, CaS phases are present on the edges, i.e., on the steel–NMI interfaces, appearing as lighter shade in the BSE image. TiN is observed in lesser amounts in the elemental maps. After 120 minutes at 900 °C, the most notable observation is the disappearance of the CaS phase of the upper part of the left side of the NMI. After additional 150 min heat treatment at 900°C, almost all of the initial CaS phase has disappeared, and clear voids have formed around the inclusion. In addition, according to the EDS maps, calcium-based matter has accumulated near the steel–NMI interfaces. The primary oxide phases, calcium aluminate and $MgAl_2O_4$ spinel, seem not to have reacted during the experiments and the compositions determined in several zones remain the same before and after the heat treatment.

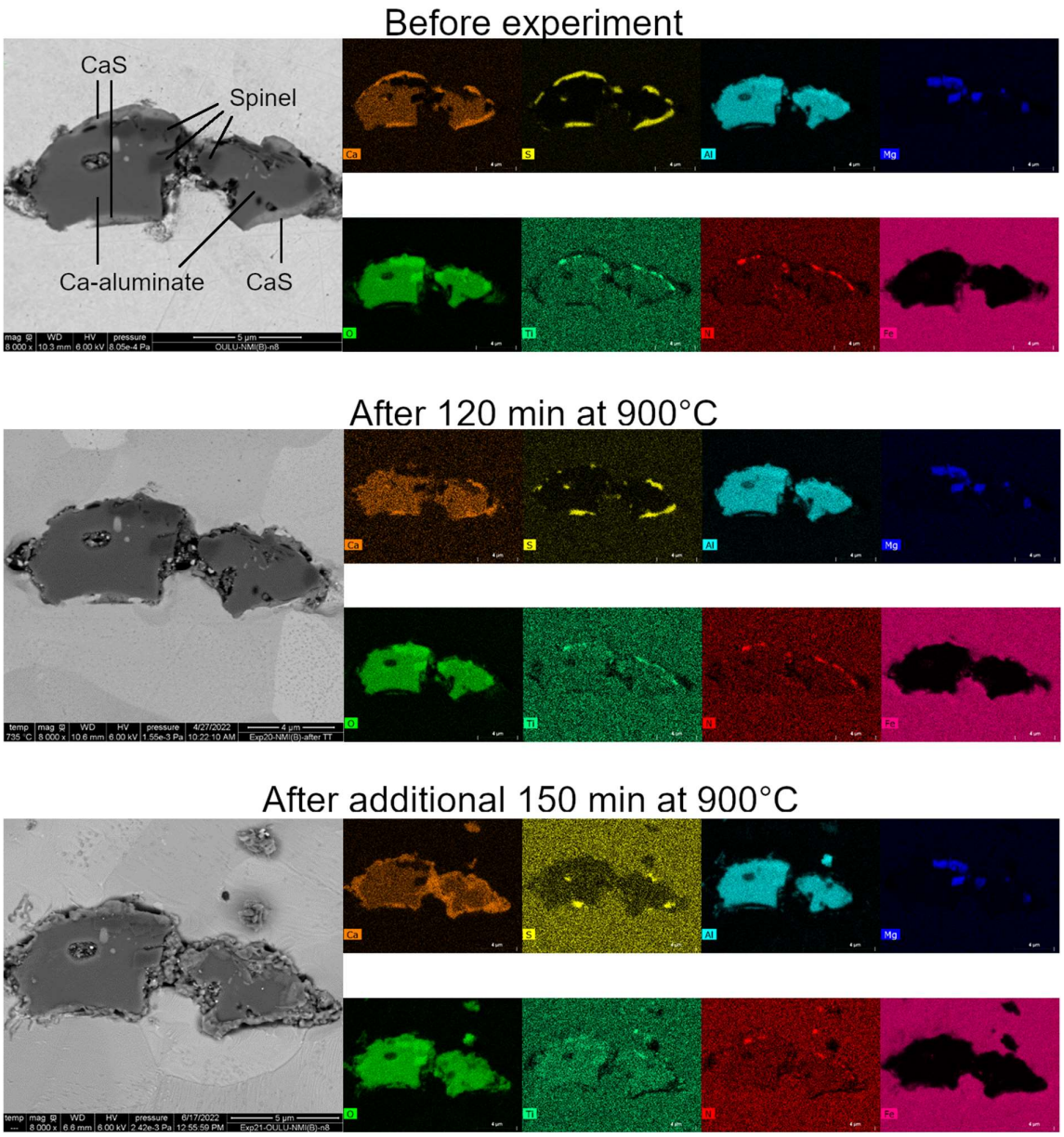

Figure 1. Complex calcium aluminate NMI before and after experiment, BSE images and elemental maps.

3.1.2 CaS type

The elemental analyses of the CaS inclusions indicate that they can contain minor amounts of MnS as solid solution. No variation in the shape and composition of CaS was observed during a 120-minute experiment at 800°C, as presented in Figure 2. Small drops of metallic iron formed rapidly at the NMI surface after the sample reached the experimental temperature. These drops can form at the CaS inclusion surface in the middle of the inclusion, as well as on the border of the inclusions. Movement on the inclusion surface during the heat treatment and merging when two drops contacting were also observed, as observed in the supplementary videos. Some metallic iron spread on the NMI surface is observed in the after-experiment BSE image in Figure 2.

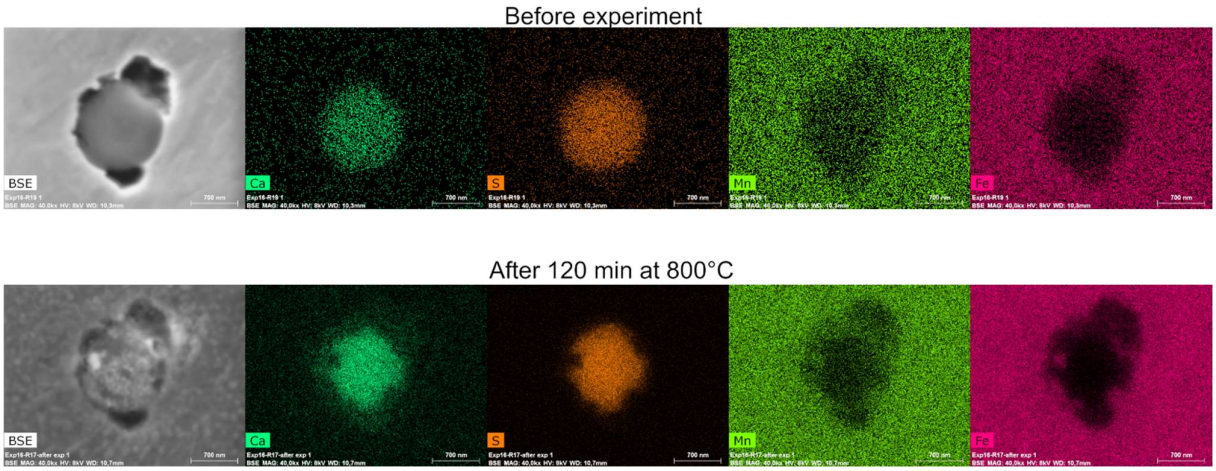

Figure 2. CaS type NMI before and after experiment, BSE images and elemental maps

3.1.3 $MgAl_2O_4$ Spinel + CaS type

Backscattered electron images and elemental maps before and after experiment at 800°C for 30 minutes are presented in Figure 3 for the NMI of this type. In the observed NMI, the lighter shade phase is CaS, and the darker one is $MgAl_2O_4$ spinel. According to the elemental mapping, TiN is observed as minor phase on the lower part of the NMI, i.e., precipitated on the surface of the oxide–sulphide type inclusion. According to the BSE imaging or elemental mapping, no clear visible changes were observed within the NMI.

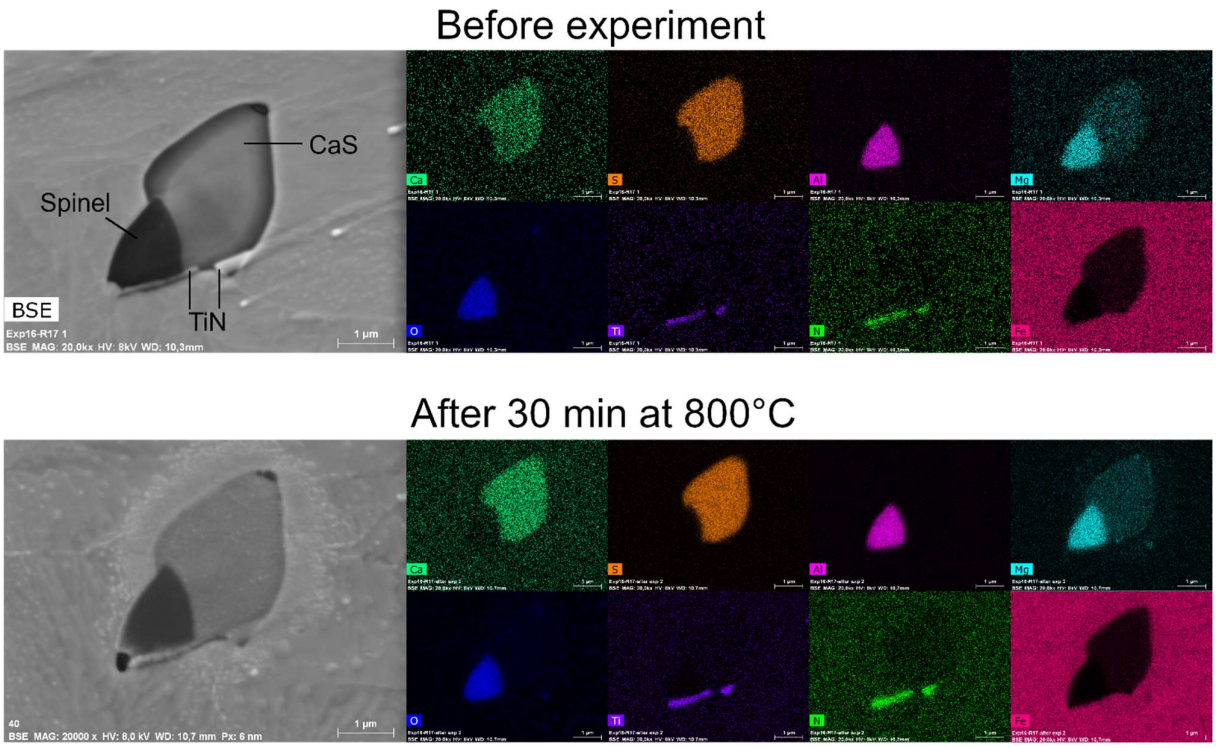

Figure 3. Spinel–CaS type NMI before and after experiment, BSE images and elemental maps.

In Figure 4, BSE image and elemental maps are presented for spinel–CaS type NMI before and after the experiments at 900°C for 30 minutes. Quite similarly, CaS and spinel phases are observed as distinct shades, and a minor amount of TiN, again on the surface of the inclusion. The NMI phases appear unchanged. However, according to the BSE images and elemental maps, the steel matrix has flown over the NMI edges.

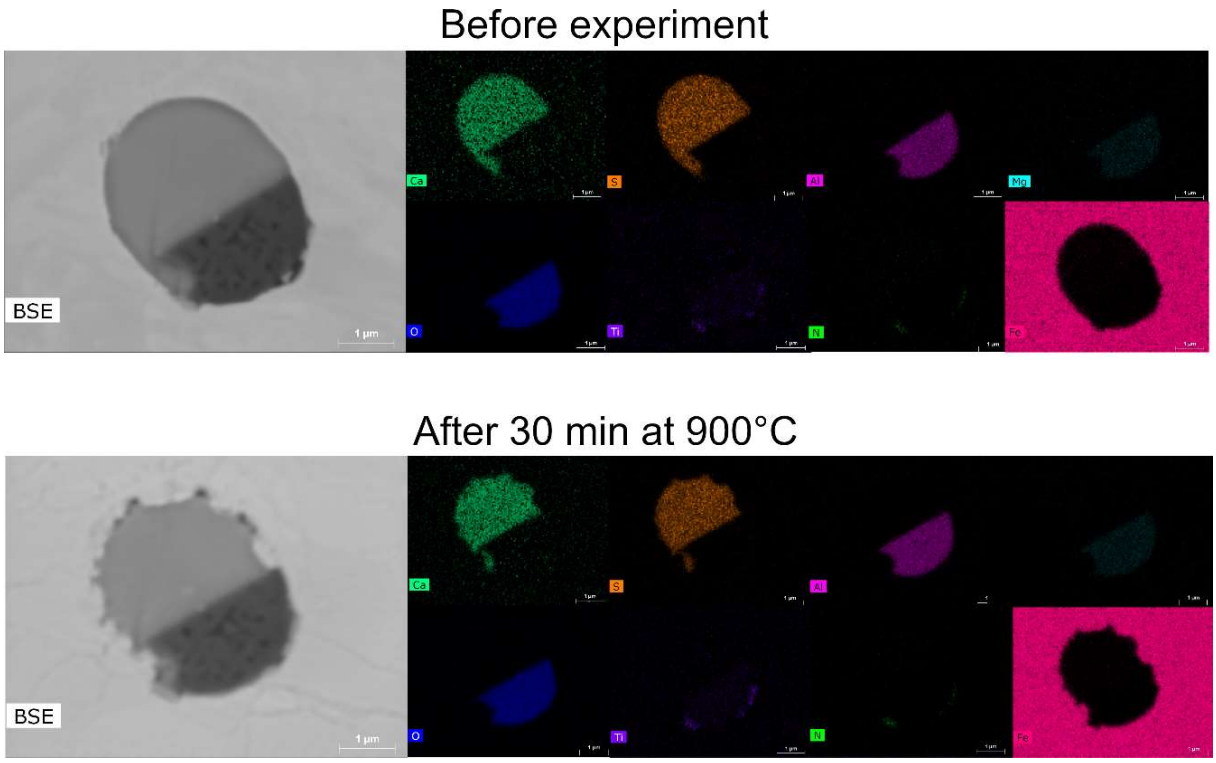

Figure 4. Spinel–CaS type NMI before and after experiment, BSE images and elemental maps.

3.1.4 TiN type

TiN type NMIs were observed in two experiments, held for 30 minutes at 800 and 900°C, results presented in Figures 5 and 6, respectively. They illustrate the observed BSE images as well as elemental maps before and after the experiments. Both BSE images and elemental maps show no observable differences within the experiments, although some iron-containing material formed on the surface in the experiment carried out at 900°C, clearly seen in the supplementary material.

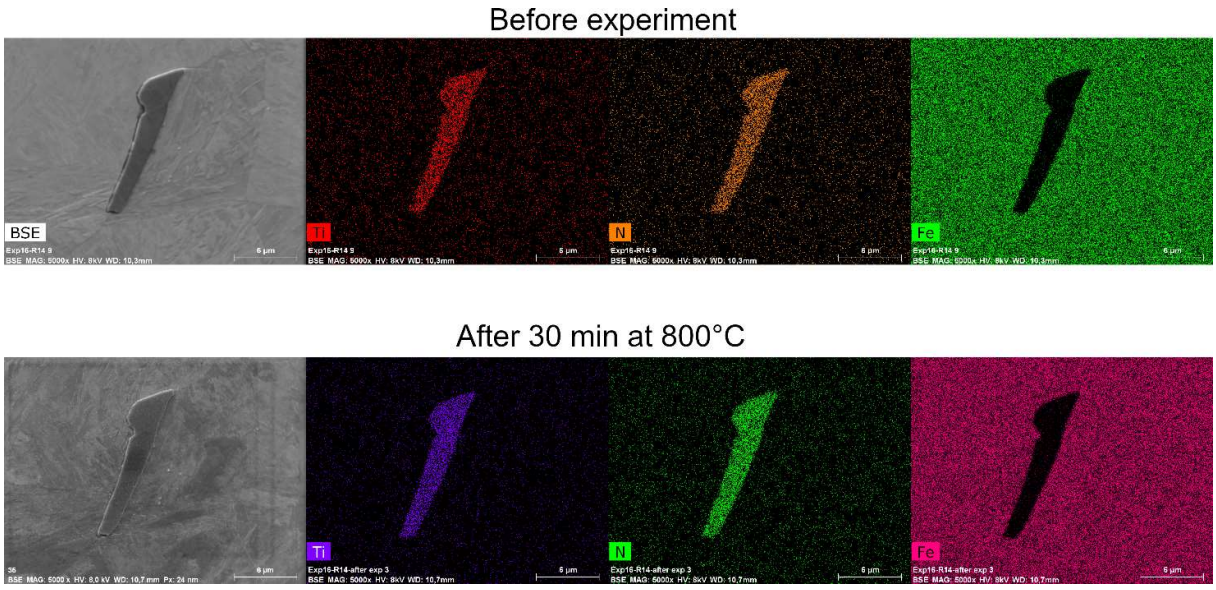

Figure 5. TiN type NMI before and after experiment, BSE images and elemental maps.

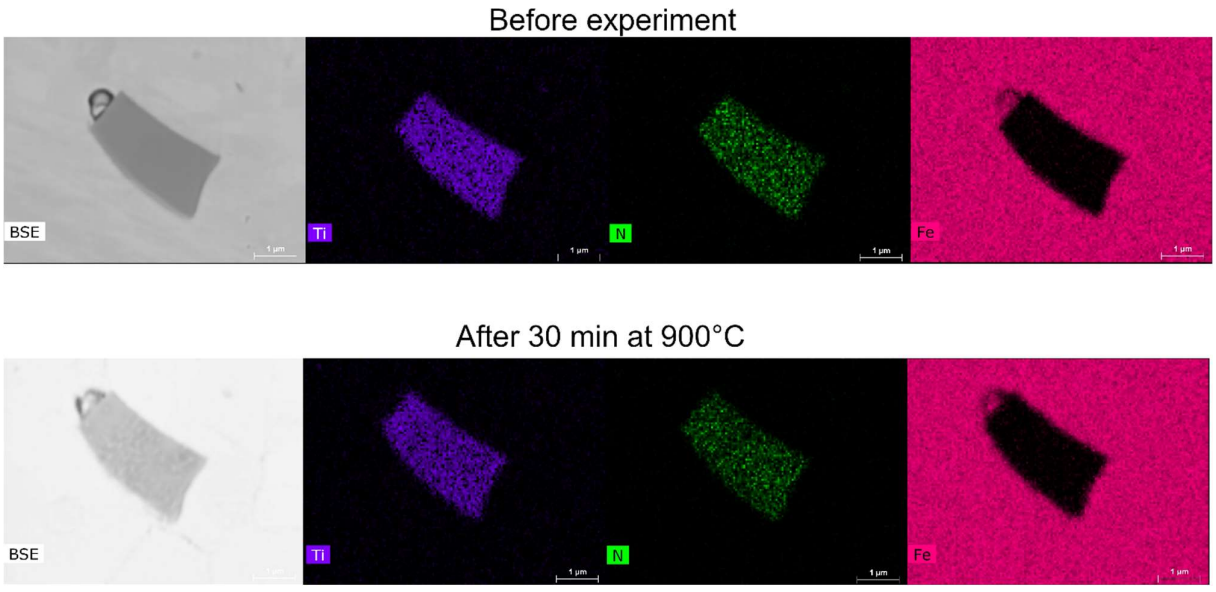

Figure 6. TiN type NMI before and after experiment, BSE images and elemental maps.

3.1.5 MnS type

As presented in Figure 7, a MnS type NMI was characterised before and after an experiment with a holding time of 30 minutes at 900°C. After the experiment, void formation was observed in the centre part, and thinning of the visible NMI in the upper part. The elemental mapping with overlapping Mn, S and Fe – area pointed with single-headed arrows in Figure 7 – suggests that in the upper part the observed thinning is caused by the flowing steel on the NMI surface rather than contraction of the NMI. On the other hand, the width of the Fe-free zone, designated with two-headed arrows, has remained constant in the centre part. In other words, the voids observed are caused by the reactions occurring in the NMI.

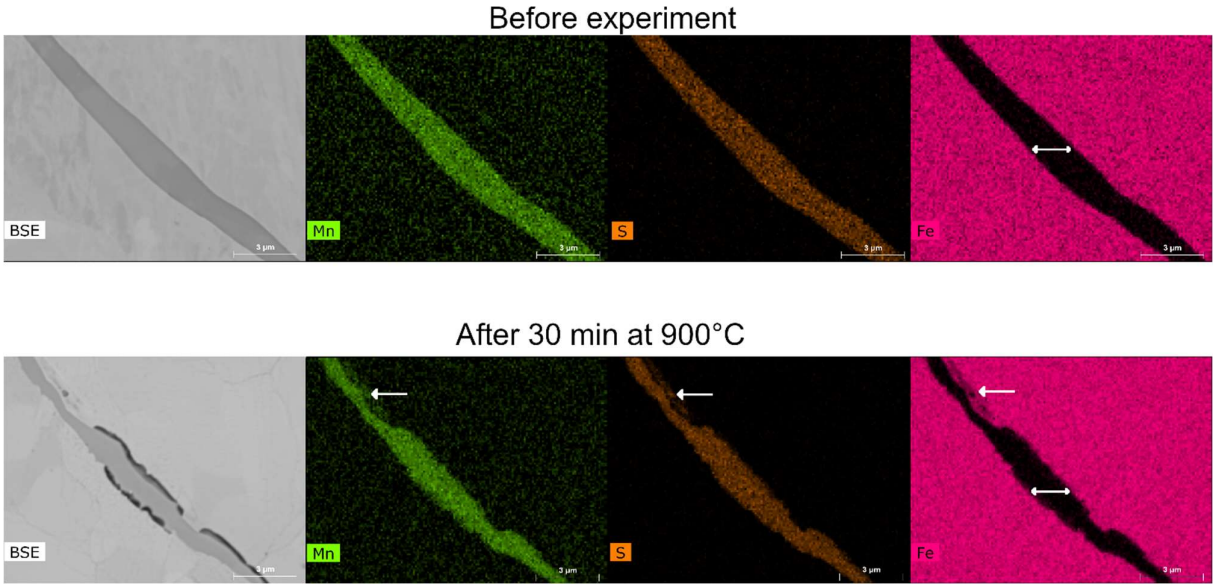

Figure 7. MnS type NMI before and after experiment, BSE images and elemental maps.

3.2 Thermodynamic assessment

The resulting partial pressures of Ca, Mn, Mg, and Ti in equilibrium according to the equations reported in Table 1 are presented in Fig. 8. They have been calculated in the temperature domain considered in the present study. The higher the curve on the graph, the higher the thermodynamic driving force for the reaction occurring from left to right. According to these results, MnS is the most likely compound to react with H_2 or to volatilise during HT-ESEM imaging. In fact, the equilibrium p_{Mn} value for MnS volatilisation reaches the system pressure (10^{-9} bar) at around 950°C. According to these results, MgO is more likely to react with the residual H_2 compared to the volatilisation reaction. CaS can be considered more stable than MnS and MgO, but less stable than calcium aluminate $CaAl_2O_4$, spinel $MgAl_2O_4$ and TiN.

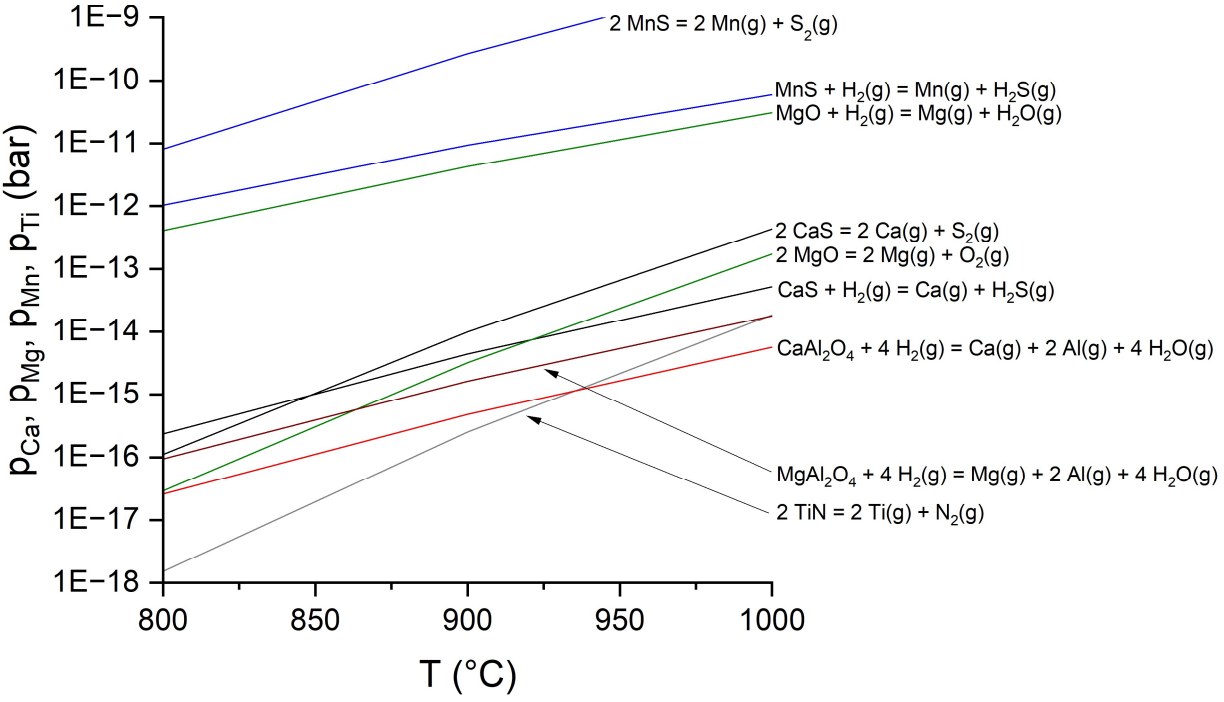

Figure 8. Partial pressures of gaseous Ca, Mn, Mg, and Ti in equilibrium under the investigated conditions.

4. Discussion

The direct observation of the NMI phases using HT-ESEM has enabled to highlight various NMI chemical reactions and morphological transformations, e.g. void formation and steel matrix flowing, that can be discussed in the light of the thermodynamical calculations or phase transformations.

4.1 Chemical reactivity

The direct observation of the CaS phases do not show any reaction occurring at 800 and 900°C during the first 30-minute holding time. Increasing the holding time to 120 and 270 minutes at 900°C yielded to the observation of CaS phase morphological modifications, corresponding to significant CaS phase reactivity in these experimental conditions. According to the thermodynamic assessment, CaS can be considered more stable than MnS and MgO, but less stable than calcium aluminate, spinel, or titanium nitride. This is in line with the HT-ESEM observations. The experimental results indicate that the kinetics of CaS decomposition remain relatively low at 900°C as reactions involving CaS were not observed with other NMIs with shorter holding times. No other chemical transformations have been observed in the different NMIs, indicating that they are stable in the experimental conditions or that the transformation kinetics are very low.

4.2 Steel matrix flowing

The MnS exhibited flowing of the steel matrix over the observed cross section of the NMI (Fig. 7). This can be attributed to the local variances in the grain structure of the steel matrix and its softening behaviour during heat treatments. A similar phenomenon was observed with a spinel–CaS type inclusion at 900°C (Fig. 4), however not at 800°C with a similar NMI (Fig. 3). During the experiment performed at 800°C, metallic iron droplets were formed on the surface of a CaS NMI (Fig. 2). As observed in the supplementary video format material, the droplets were observed to be mobile at the CaS surface, illustrating the non-wetting properties between the NMIs and softened steel. Formation of iron-rich material was also observed on the surface on TiN at 900°C, but their shape was string-like rather than spherical.

4.3 Void formation

Void formation on the steel matrix–NMI boundary was observed with a complex calcium aluminate NMI (Fig. 1) and with a MnS inclusion (Fig. 7). According to Kiessling & Lange [16], sulphides are the most prone void forming NMIs, owing to their large thermal expansion coefficient, suggesting void formation during cooling to room temperature. In the present study, void formation is observed to occur at high temperature, during the isothermal treatment of the sample, and not after sample cooling at room temperature. Thus, in this case, the difference of the NMIs and matrix thermal expansion coefficients is not the reason for the void formation. Instead, it can only be attributed to high temperature reactivity.

First, the phase transformations in the steel matrix may have a role on the void formation. FactSage calculations with FSstel database show that the transition temperature for the studied steel composition (0.15C–0.3Si–1.0Mn–0.4Cr) is 825°C, i.e., above that temperature the microstructure is fully austenitic, whereas below that temperature both austenite and ferrite are stable. In the experiments conducted at 800°C, a fraction of the steel matrix is assumed to be austenitic. In the experiments at 900°C, the microstructure has undergone a complete phase transformation, the

volume contraction of which is approximately one percent and this can be one reason for the observation of void formation [17].

Second, according to thermodynamic considerations, the volatilisation reaction of MnS results in partial pressure of manganese close to the HT-ESEM system pressure at around 950°C, indicating that MnS volatilisation could be another probable cause for the observed shrinkage of MnS. The reaction of MnS with H_2 results in slightly lower equilibrium p_{Mn}, still several magnitudes higher than equilibrium p_{Ca} values for CaS reacting with H_2 or volatilisation. This indicates a higher reactivity of MnS compared to CaS in the experimental conditions with both reaction routes, observed as void formation with the MnS NMIs.

4.4 Implications for HT-ESEM analyses

In the present study, in-situ HT-ESEM experiments with steel samples have been performed to observe various NMI reactions for the first time. The technique has enabled the direct sub-micrometer scale observation of local transformations at 800 and 900°C. The continuous recording of images in the same region of interest, coupled with ex-situ EDS mapping performed before and after the experiment, yielded to evidence chemical reactions, void formation and steel matrix flowing. Furthermore, partial oxidation of the steel matrix has not been observed along the experiments, indicating that the combination of the FurnaSEM stage with the Karmen detector are particularly well adapted for this type of studies. However, one should note that although the technique suits well with the study of such phenomena, the covering of the NMI particles by the steel matrix flowing limits its use to the study of processes where the area of interest remains accessible to the electron beam and is not masked.

5. Conclusion

The current study presents results of in-situ observation of non-metallic inclusions in steel with high-temperature environmental scanning electron microscopy. The reactions occurring in calcium aluminate, CaS, $MgAl_2O_4$–CaS, MnS, and TiN type NMIs were observed at 800°C and 900°C with varying holding times. The main findings can be summarised as follows:

1. Decomposition of CaS was observed in the case of complex calcium aluminate NMI held at 900°C for a total of 120+150 minutes, but not with shorter holding times at target temperatures, indicating a low rate of transformation kinetics.
2. Void formation around NMIs was observed at 900°C with a calcium aluminate containing CaS and with a MnS type NMI. Possible causes are contraction during the ferrite–austenite phase transformation, and according to thermodynamic considerations, MnS volatilisation or reaction with the residual atmosphere.
3. Flowing of the steel matrix onto the NMI was observed at 900°C experiments with spinel–CaS and MnS type NMIs, attributed to softening of steel during heat treatments.
4. Based on the current investigation, the applicability of HT-ESEM to in-situ high temperature NMI imaging is adapted to the study of inclusion phase transformations in the prevailing conditions, and moderate temperatures, but can remain limited due to steel matrix flowing and partial covering of the NMIs.

Acknowledgements

Sample preparation by Mr. Tun Tun Nyo with University of Oulu is greatly appreciated by the authors.

Declarations

Author contribution statement

T. Alatarvas: Conceptualisation, thermodynamic calculations, writing – original draft preparation.

R. Podor: Carrying out the experiments, writing – review and editing.

Q. Shu: Conceptualisation, writing – review and editing.

E.-P. Heikkinen: Thermodynamic calculations, writing – review and editing.

H. Singh: Coordination, conceptualisation, writing – review and editing.

Funding statement

This research is a part of the CLEAN2STEEL project that benefits from the financial and strategic support of the Kvantum Institute, University of Oulu.

Data availability statement

Data is not shared.

Declaration of interests statement

The authors declare no conflict of interest.

References

[1] Y. Sahai, T. Emi, Tundish Technology for Clean Steel Production, (2008) World Scientific, https://dx.doi.org/10.1142/6426.

[2] H. Tervo, A. Kaijalainen, T. Pikkarainen, S. Mehtonen, D. Porter, Effect of impurity level and inclusions on the ductility and toughness of an ultra-high-strength steel, Mater. Sci. Eng. A 697 (2017) 184-193, http://dx.doi.org/10.1016/j.msea.2017.05.013.

[3] G. Cheng, W. Li, X. Zhang, L. Zhang, Transformation of Inclusions in Solid GCr15 Bearing Steels During Heat Treatment, Metals 9 (2019) 642, http://dx.doi.org/10.3390/met9060642.

[4] Y. Chu, W. Li, Y. Ren, L. Zhang, Transformation of Inclusions in Linepipe Steels During Heat Treatment, Metall. Mater. Trans. B 50 (2019) 2047-2062, https://doi.org/10.1007/s11663-019-01593-1.

[5] J. Wang, L, Zhang, G. Cheng, Y. Zhang, Q. Ren, Kinetic Prediction for Isothermal Transformation of Inclusions in a Bearing Steel, Metall. Mater. Trans. B 53 (2022) 394-406, https://doi.org/10.1007/s11663-021-02375-4.

[6] C. Liu, B. Webler, Evolution of non-metallic inclusions during heat treatment, Metall. Res. Technol. 117 (2020) 408, https://doi.org/10.1051/metal/2020040.

[7] C. Liu, B. Webler, Thermodynamic and Kinetic Analyses of Inclusion Transformations in Linepipe Steel during Isothermal Heating at 1473 K (1200 °C), Steel Res. Int. 94 (2023) 2200556, https://doi.org/10.1002/srin.202200556.

[8] H. Liu, W. Li, C. Ren, L. Zhang, Y. Ren, Inclusion Evolution in Al-Killed Ca-Treated Steels at Heat Treatment Temperature In Situ Observed Using Confocal Scanning Laser Microscope, Metall. Mater. Trans. B 53 (2022) 1323-1328, https://doi.org/10.1007/s11663-022-02472-y.

[9] R. Podor, G. I. Nkou Bouala, J. Ravaux, J. Lautru, N. Clavier, Working with the ESEM at high temperature, Mater. Charact. 151 (2019) 15-26, https://doi.org/10.1016/j.matchar.2019.02.036.

[10] M. Barreau, C. Méthivier, T. Sturel, C. Allely, P. Drillet, S. Cremel, R. Grigorieva, B. Nabi, R. Podor, J. Lautru, V. Humblot, J. Landoulsi, X. Carrier, In situ surface imaging: High temperature environmental SEM study of the surface changes during heat treatment of an Al–Si coated boron steel, Mater. Charact. 163 (2020) 110266 https://doi.org/10.1016/j.matchar.2020.110266.

[11] S. Poitel, Z.-J. Wang, M. G. Willinger, J. Van Herle, C. Hébert, In-situ Observation of Co-Ce Coated Metallic Interconnect Oxidation Combined with High-Resolution Post Exposure Analysis, ECS Trans. 78 (2017) 1615-1632, https://doi.org/10.1149/07801.1615ecst.

[12] R. Podor, X. Le Goff, J. Lautru, H.P. Brau, M. Barreau, X. Carrier, J. Mendonça, D. Nogues, A. Candeias, Direct Observation of the Surface Topography at High Temperature with SEM, Microsc. Microanal. 26 (2020) 397-402, https://doi.org/10.1017/S1431927620001348.

[13] R. Podor, J. Mendonça, J. Lautru, H.P. Brau, D. Nogues, A. Candeias, P. Horodysky, A. Kolouch, M. Barreau, X. Carrier, N. Ramenatte, S. Mathieu, M. Vilasi, Evaluation and application of a new

scintillator-based heat-resistant back-scattered electron detector during heat treatment in the scanning electron microscope, J. Microsc. 282 (2021) 45-59, https://doi.org/10.1111/jmi.12979.

[14] C.W. Bale, E. Bélisle, P. Chartrand, S.A. Decterov, G. Eriksson, K. Hack, I.-H. Jung, Y.-B. Kang, J. Melançon, A.D. Pelton, C. Robelin, S. Petersen, FactSage thermochemical software and databases – recent developments, Calphad 33 (2009) 295-311, http://dx.doi.org/10.1016/j.calphad.2008.09.009.

[15] A. Schopphoff, F. Braunschweig, Generation of UHV with Turbomolecular Pump and Dry Backing Pump: Meeting the demand for completely hydrocarbon-free vacuum, Vak. Forsch. Prax. 29 (2017) 22-25, https://doi.org/10.1002/vipr.201700659.

[16] R. Kiessling, N. Lange, Non-metallic inclusions in steel, Second edition (1978), The Metals Society. ISBN 0-904357-18-X.

[17] S. Louhenkilpi, Continuous Casting of Steel, in: S. Seetharaman (Ed.) Treatise on Process Metallurgy, Volume 3 (2014), Elsevier, https://doi.org/10.1016/B978-0-08-096988-6.00007-9.

List of Figures

List of Tables